Eur. Phys. J. D **40**, 369–375 (2006)
DOI: 10.1140/epjd/e2006-00170-7

THE EUROPEAN PHYSICAL JOURNAL D

Scattering of electrons from gas-phase $N_2O(^1\Sigma)$: Computed cross-sections and angular distributions in comparison with experiments

F.A. Gianturco[1,a] and T. Stoecklin[2]

[1] Department of Chemistry, The University of Rome La Sapienza and CNISM, Piazzale A. Moro 5, 00185 Rome, Italy
[2] Laboratoire de Physico-Chimie Moleculaire, 351 cours de la Libération, 33405 Talence, France

Received 4 May 2006 / Received in final form 14 June 2006
Published online 14 July 2006 – © EDP Sciences, Società Italiana di Fisica, Springer-Verlag 2006

Abstract. Ab initio calculations are reported for the quantum scattering of electrons from N_2O molecules in the gas phase and for energies which range from near threshold up to about 100 eV. Elastic integral cross-sections and angular distributions are examined in detail and an extensive comparison is made with existing experiments. The agreement found with the latter data is fairly good and results are further discussed to explain the physical mechanisms at work for this polar target.

PACS. 34.80.Bm Elastic scattering of electrons by atoms and molecules – 34.80.-i Electron scattering

1 Introduction

The nitrons oxide (N_2O) gaseous molecule is one of the simplest, stable triatomic molecules of linear structure which has been the subject of several experimental and computational studies in recent years [1–6]. Since it is believed to play a significant role in the chemistry of the ozone layer, and in the chemistry of the upper atmosphere in general, its study from the point of view of establishing the dynamics of electron attachment processes were indeed started several years ago (e.g. see [6]) and the interest remained high because of its several technological applications involving cold plasmas. The experimental studies [1,5,6] have also found that the position and width of the narrow shape resonances like the one located near 2.3 eV are very sensitive to various aspects of the measurements and therefore have proven to be difficult to study systematically from the computational viewpoint, since they are markedly affected, among other things, by the neglect of vibrational motion [2–4]. Such studies have produced low-energy measurements in the nineties [7,8] and even earlier analysis using electron beam attenuation techniques have been applied to this molecule [6,9,10].

In the present theoretical study our main objectives have been the following:

- to analyse with an exact static-exchange (ESE) treatment and a model polarisation potential the form and location of the main, low-energy shape resonance mentioned above;
- to compare new calculations with the existing angular distribution data over a fairly broad range of collision energies and for the largest possible range of angles;
- to estimate for this polar molecular target the form of the energy dependence, at specific scattering angles, of the electron distributions in the elastic channels.

The work is organized as follows: Section 2 reports an outline of our theoretical machinery while Section 3 presents our results and analyses them. Our conclusions are collected in Section 4.

2 The theoretical modelling

If one adopts a one-electron picture for the description of the elastic scattering process in the fixed-nuclei limit, one finds that the collision is determined by an effective Hamiltonian

$$H_{eff} = T + U \tag{1}$$

where T denotes the kinetic energy of the scattered electron and U denotes some optical potential. The latter can be obtained in a variety of ways and its function has often been discussed in the literature [13]. Within the exact static exchange+polarization (ESEP) approximation, the simplest useful approximation to U, one splits it in a local and non-local term, the former being real, energy independent and long ranged while the latter is short ranged and energy-dependent,

$$U(\mathbf{r}, \mathbf{r}', E) = V(\mathbf{r})\,\delta(\mathbf{r} - \mathbf{r}') + W(\mathbf{r}, \mathbf{r}', E) \tag{2}$$

where $\mathbf{r}$ and $\mathbf{r}'$ label two arbitrary electron coordinates. All the nuclear coordinates are not explicitly indicated

[a] e-mail: fa.gianturco@caspur.it

and are supposed here to be fixed at their equilibrium values (the FN approximation).

In the present case, the distances adopted were those of the molecular equilibrium geometry: $R_{\rm NN} = 2.132a_0$; $R_{\rm NO} = 2.2378a_0$ and the chosen basis set expansion for the target molecular orbitals (MO's) was the valence double zeta D95V* following the standard notation of the quantum expansion in Gaussian orbitals [14]. Whenever the scattering process could take place with an 'undistorted' molecular charge distribution and the polarization-correlation effects were disregarded, then the local potential V becomes the static interaction, where $\mathbf{r}_e$ identifies the scattered electron coordinate

$$V(\mathbf{r}_e) = 2\sum_j \int d\mathbf{r} \frac{|\varphi_j(\mathbf{r})|^2}{\mathbf{r}-\mathbf{r}_e} - \sum_k \frac{Z_k}{|\mathbf{r}-\mathbf{R}_k|} \tag{3}$$

and W becomes the exchange interaction without any dependence on the projectile relative energy

$$W(\mathbf{r},\mathbf{r}_e,E) = -\sum_j \frac{\varphi_j(\mathbf{r})\varphi_j(\mathbf{r}_e)}{|\mathbf{r}-\mathbf{r}_e|} \tag{4}$$

with both sums running over the number N of bound electrons of the target and $\mathbf{r}_e$ is now the coordinate of the scattered electron and $\mathbf{r}$ represents the coordinate of a bound electron. In the above equations $\{\phi_j\}$ denotes the set of doubly occupied self-consistent-field (SCF) orbitals, while $\{R_k\}$ and $\{Z_k\}$ denote the sets of nuclear positions and charges, respectively.

The first step is therefore that of solving the scattering problem for the local and long range potential V. This will be done, as mentioned below, by solving coupled integral equations by a finite-step method. The residual scattering due to the non-local interaction could be done within the T-matrix expansion approach since, due to the short-range character of the exchange potential, W can be quite well represented via the use of a separable approximation [15,16]. Thus we start by approximating the exchange potential W by the truncated separable form:

$$W(\mathbf{r},\mathbf{r}_e) \approx \sum_{\alpha,\beta}^{N} \chi_\alpha(\mathbf{r}) W_{\alpha,\beta} \chi_\beta(\mathbf{r}_e) \tag{5}$$

where the $\{\chi\}$ are now additional, new Cartesian Gaussian functions not necessarily orthogonal to each other, nor to the occupied molecular orbitals of the target SCF basis set mentioned before: they are meant to describe the scattered electron within the bound electron density spatial region. We shall describe them in the next section.

The exchange matrix elements for the bound orbitals of the molecule are given by first calculating the following matrix elements

$$\tilde{K}_{\gamma\tau} = \int d\mathbf{r} \int d\mathbf{r}_e \varphi_\gamma(\mathbf{r}) W(\mathbf{r},\mathbf{r}_e) \varphi_\tau(\mathbf{r}_e) \tag{6}$$

hence

$$\tilde{K}_{\gamma\tau} = \sum_{\alpha,\beta} \int d\mathbf{r} \varphi_\gamma(\mathbf{r}) \chi_\alpha(\mathbf{r}) W_{\alpha,\beta} \int d\mathbf{r}_e \varphi_\tau(\mathbf{r}_e) \chi_\beta(\mathbf{r}_e) \tag{7}$$

and

$$\tilde{K}_{\gamma\tau} = \sum_{\alpha,\beta} S_{\gamma\alpha} W_{\alpha,\beta} S_{\beta\tau} \tag{8}$$

we are finally looking for the exchange matrix $\mathbf{W}$ as given by

$$\mathbf{W} = \mathbf{S}^{-1} \tilde{\mathbf{K}} \mathbf{S}^{-1} \tag{9}$$

with $S_{\alpha\beta}$ being the overlap matrix elements.

Within a single-center expansion (SCE) of the continuum wavefunction and of the interaction potential, the use of the exact-static-exchange (ESE) approximation gives rise to a set of coupled integro-differential equations [11] over the radial variable r_e describing the scattered electron, with u_{ll_0} describing the radial part of the scattering wavefunction

$$\left\{\frac{d^2}{dr_e^2} + \frac{l(l+1)}{r_e^2} + k^2\right\} u_{ll_0}(r_e) = \sum_{l'} \left\{ U_{ll'}(r_e) u_{l'l_0}(r_e) + \sum_{\alpha\beta} \Phi_\alpha^\ell(r_e) W_{\alpha\beta} \int dr \Phi_\beta^\ell(r) u_{l'l_0}(r) \right\} \tag{10}$$

where r describes any of the N-bound electrons and

$$U_{ll'}(r_e) = \int S_l^m(\hat{\mathbf{r}}_e) V(\mathbf{r}_e) S_l^m(\hat{\mathbf{r}}_e) d\hat{\mathbf{r}}_e \tag{11}$$

and

$$\Phi_\alpha^\ell(r_e) = (r_e) \int d\hat{\mathbf{r}}_e \varphi_\alpha(\mathbf{r}_e) S_l^m(\hat{\mathbf{r}}_e) \tag{12}$$

which integrates over real spherical harmonics $S_l^m(\hat{r}_e)$ to yield the radial part of each new function: here the φ_α are the φ_j orbitals we discuss in equation (4). Furthermore, each S_l^m carries a parity index p, defined below, which we have dropped above for simplicity of notation

$$S_l^{m,p}(\hat{\mathbf{r}}_e) = \frac{i}{\sqrt{2}} \{ Y_l^m(\hat{\mathbf{r}}_e) \pm (-1)^p Y_l^{-m}(\hat{\mathbf{r}}_e) \} \tag{13}$$

with the parity index $p = 0$ or 1.

One can now express the solution as a linear combination of homogeneous and inhomogeneous terms:

$$u_{ll_0}(r_e) = u_{ll_0}^0(r_e) + \sum_\alpha u_l^\alpha(r_e) C_{l_0}^\alpha \tag{14}$$

where

$$\left(k^2 - H_0^\ell\right) u_{ll_0}^0(r_e) = \sum_{l'} U_{ll'}(r_e) u_{l'l_0} \tag{15}$$

$$\left(k^2 - H_0^\ell\right) u_l^\alpha(r_e) = \sum_{l'} U_{ll'}(u_{l'}^\alpha) + \Phi_\alpha^\ell. \tag{16}$$

The coefficients C_l^α are found to satisfy a set of linear equations

$$\sum_\beta A_{\alpha\beta} C_{l_0}^\beta = B_{\alpha l_0} \tag{17}$$

where

$$A_{\alpha\beta} = \delta_{\alpha\beta} - \sum_{l'\gamma} W_{\alpha\gamma} \int \Phi_\gamma^{\ell'}(r_e) u_{l'}^\beta(r_e) dr_e \tag{18}$$

Table 1. Gaussian orbital exponents for the separable exchange kernels.

Σ	Π	Δ
(location, type, expt.s)	(location, type, expt.s)	(location,type, expt.s)
on N:	**on N**:	**on N**:
s: (4.0, 2.0, 1.0, 0.5, 0.25)	$\mathbf{p_x}$: (32.0, 16.0, 8.0, 4.0, 2.0, 1.0, 0.5)	$\mathbf{d_{xx}}$: (16.0, 8.0, 4.0, 2.0, 1.0, 0.5, 0.25)
$\mathbf{p_z}$: (4.0, 2.0, 1.0, 0.5)	$\mathbf{d_{xz}}$: (4.0, 2.0, 1.0, 0.5, 0.25)	$\mathbf{f_{x^2z}}$: (4.0, 2.0, 1.0, 0.5, 0.25)
$\mathbf{d_{zz}}$: (1.0, 0.5)		
on O:	**on O:**	**on O:**
s: (4.0, 2.0, 1.0, 0.5, 0.25, 0.1)	$\mathbf{p_x}$: (32.0, 16.0, 8.0, 4.0, 2.0, 1.0, 0.5)	$\mathbf{d_{xx}}$: (16.0, 8.0, 4.0, 2.0, 1.0, 0.5, 0.25)
$\mathbf{p_z}$: (4.0, 2.0, 1.0, 0.5, 0.25, 0.1)	$\mathbf{d_{xz}}$: (4.0, 2.0, 1.0, 0.5, 0.25)	$\mathbf{d_{xz}}$: (4.0, 2.0, 1.0, 0.5, 0.25)
$\mathbf{d_{zz}}$: (1.0, 0.5)		
	at center of mass:	**at center of mass**:
	$\mathbf{p_x}$: (32.0, 16.0, 8.0, 4.0, 2.0, 1.0, 0.5)	$\mathbf{d_{xx}}$: (16.0, 8.0, 4.0, 2.0, 1.0, 0.5, 0.25)
	$\mathbf{d_{xz}}$: (4.0, 2.0, 1.0, 0.5, 0.25)	$\mathbf{f_{x^2z}}$: (4.0, 2.0, 1.0, 0.5, 0.25)

and

$$B_{\alpha l_0} = \sum_{l'\beta} W_{\alpha\beta} \int_0^0 \Phi_\beta^{l'}(r_e) u_{l'l_0}^0(r_e) dr_e. \qquad (19)$$

The final numerical integration of the ensuing Volterra equations was then carried out exactly as already described in our previous work [11].

2.1 The interaction forces

2.1.1 The static potential

The wavefunction of the target was taken to be the ground electronic state calculated at the SCE level, using the D95V* basis set mentioned above. This calculation was carried out at the experimental values of the interatomic distances, also given before. We obtain a quadrupole moment $Q = 3.31$ au in good agreement with the experimental value of 2.6 a.u. [17] and a dipole moment of $\mu = 0.664$ Debye larger than the experimental value of 0.16 D [18]. The analytical coefficients for the expansion of each occupied molecular orbital φ_i were given, in symmetrized, real spherical harmonics,

$$\varphi_i^m(\mathbf{r}) = \sum_l C_l^m(r) S_l^{m,p}(\theta, \phi). \qquad (20)$$

The above expansion was then used to generate the electrostatic potential:

$$V(r) = \int d\mathbf{r}' \sum_i \frac{\varphi_i^m(\mathbf{r}) \varphi_i^{m*}(\mathbf{r}')}{|\mathbf{r} - \mathbf{r}'|} \qquad (21)$$

and the potential was finally expanded in Legendre polynomials up to $l = 80$ for the maximum multipolar coefficients which describe the scattering potential.

2.1.2 The polarization potential

As mentioned in the introduction we used in the inner region the density functional form as given by Padial and Norcross [17]. The asymptotic part of this potential was calculated using the experimental values of the polarization: $\alpha_0 = 19.77 a_0^3$; $\alpha_2 = 12.73 a_0^3$.

2.1.3 The exchange potential

The Gaussian basis set $|\gamma_\alpha\rangle$ that we used to expand the exchange kernel is given for each symmetry in Table 1 where the meaning of the symbols is explained there.

The expansion of the orthogonalized basis set in spherical harmonics was carried out analytically by using the shifting of Gaussian functions and we took for each type of basis functions the first two contributions to this expansion. The ℓ values went up to $\ell_{max} = 20$ for Σ orbitals, up to 15 for Π orbitals and Δ orbitals. The steps of the grid for the radial coordinate were taken to be $0.005 a_0$ up to $r_e = 10 a_0$. For larger electron radial distances up to $500 a_0$ we used the asymptotic part of the static potential plus the polarization contributions which make up the full SECP interaction potential.

3 Computed scattering quantities

For the three symmetries which we have employed to describe the scattering process, the partial wave value for the continuum molecular electron was taken to run up to 50, hence using the multipolar expansion up to 80 and for λ larger than 50 only the static interaction was used. Numerical convergence of $\sim$1% for the final cross-sections was checked as a function of both angular and separable basis sets at each computed energy. The scattering amplitudes for the differential cross-sections (DCSs) were calculated correctly with the full potential up to $\ell = 30$, and beyond that value the Born correction was employed [18], reaching the same level of numerical convergence.

Figure 1 shows the energy behaviour of the eigenphase sums for the Π symmetry (upper panel) and the Σ symmetry (lower panel). One clearly sees that the present calculations exhibit the presence of a fairly narrow shape resonance around 2.0 eV while they also show that the phaseshift for the Σ component indicates a broader resonant feature around 11 eV. The corresponding comparison with existing experiments [8,9] is shown by the two panels of Figure 2, where the upper panel indicates the narrow π-resonance obtained from our calculations (solid line) and its good agreement with the measured location and width. We also report in that panel the results from

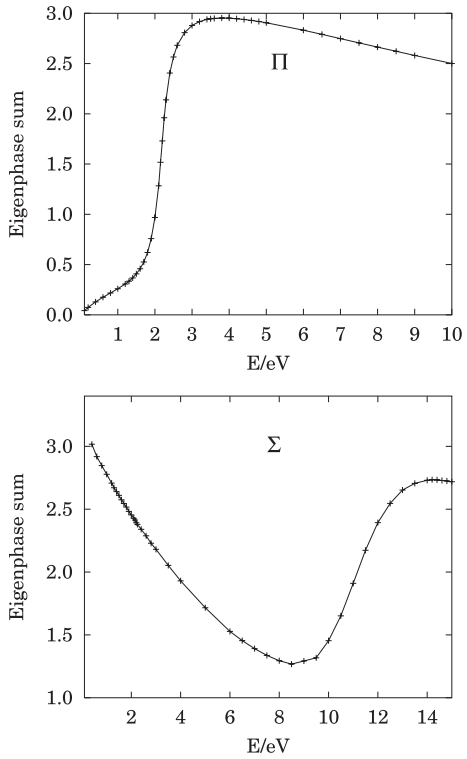

Fig. 1. Computed eigenphase sums for the elastic scattering process: see text for numerical details. Upper panel: Π symmetry; lower panel: Σ symmetry.

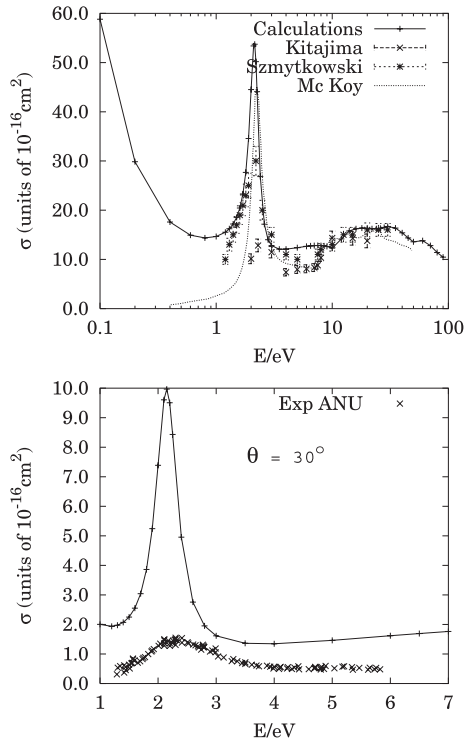

Fig. 2. Computed and measured differential integral elastic cross-sections around the resonance region. Upper panel: integral cross-section (solid line) and measurements from reference [8] (open circles) and [9] (open squares). Lower panel: electron angular distributions at $\vartheta = 30^\circ$ and as a function of collision energy. The experiments are from reference [1]. The dots report calculations from reference [2].

earlier calculations [2]. The lower panel in the same figure indicates an interesting comparison with the data recently obtained from the group in Camberra (labeled ANU in the figure) [1]. We report there the shape of the total, integral elastic cross-section at a fixed space-frame scattering angle ($\vartheta = 30^\circ$) and as a function of collision energies. The general shape of the experiments is qualitatively followed by our calculations, which also exhibit a sharp increase around 2 eV due to the location of the π-resonant state discussed before. However, due to the lack of vibrational averaging in our study we find that the marked broadening seen in the experiments is not present in the calculations, which show therefore a much narrower resonance peak.

Two further examples of the electron angular distributions after the scattering process are given in the two panels of Figure 3: we show there the experimental data of the Australian group [1] (labelled ANU) at two large-angle scattering and compare them with our calculations. It is interesting to see that theory still maintains a remnant of the resonance structure around 2 eV, while the experiments are barely able to show any sign of it in the general behaviour of the measured cross-sections. Likewise, the backscattering at 135° still shows in the calculations a marked resonance peak around 2 eV, while experiments exhibit only a broad 'hump' in that energy region. Given the fact that our theory does not include any vibrational effect, it seems reasonable to attribute the damping effect to such averaging over nuclear motions.

Given the encouraging behaviour of the computed angular distributions in comparison with experiments, we then decided to go one step further and to fully evaluate several elastic DCS's for this polar target in order to test them against existing experiments.

3.1 DCSs in the resonance region

In order to give us a more detailed knowledge on the angular distributions at energies around the prominent π-resonance, we report in Figures 4 and 5 the comparison of our calculations with the experimental differential cross-sections from the group at Sophia University [8] (SU) and from the Australian group [1] (ANU).

It is interesting to note that our calculations follow rather closely, in both size and shape, the measured cross-sections: the two panels of Figure 4, which correspond to energies lower and higher than the resonance position respectively, indicate that the backward scattering should increase around that energy but also that the forward scattering remains rather prominent as the energy increases. These two effects are also present in the experiments and our calculations are able to reproduce them rather realistically.

The data shown by Figure 5, report two additional sets of experimental data for the angular distributions: the

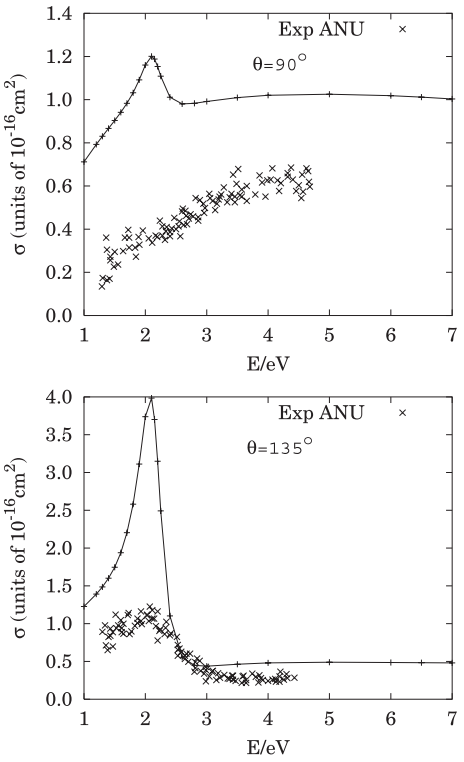

Fig. 3. Computed and measured scattered electron angular distributions at two different large-angle values: at 90° (upper panel) and at 135° (lower panel). The experiments are from reference [1].

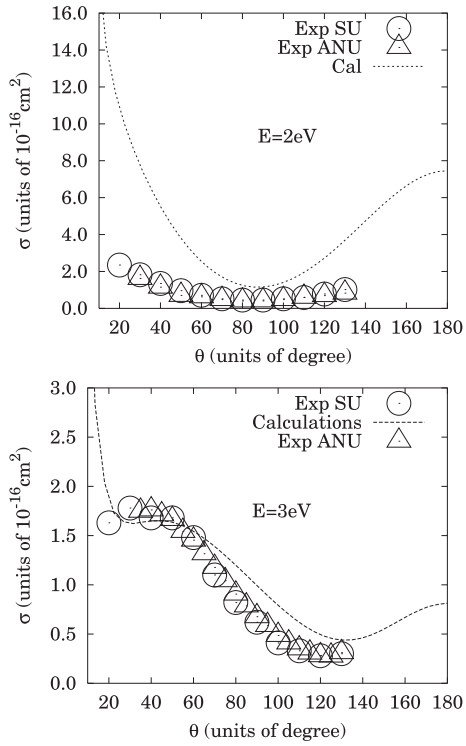

Fig. 5. Same differential cross-section data as in Figure 4 but for two different energies: at 2.0 eV (upper panel) and at 3.0 eV (lower panel). The open triangles are the experiments from reference [1].

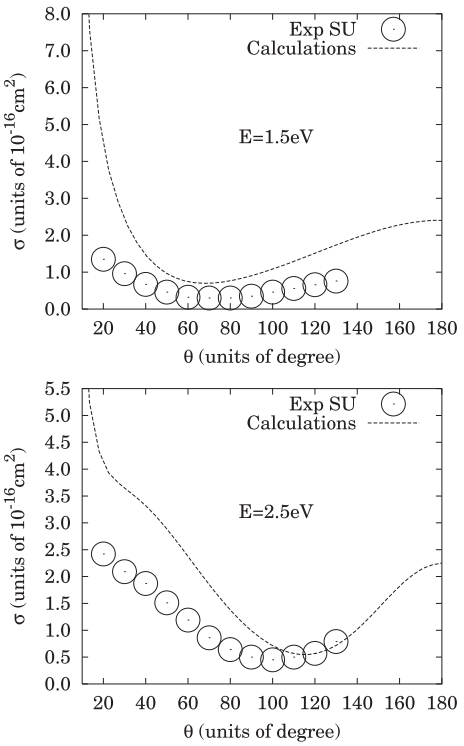

Fig. 4. Computed and measured scattered electron angular distributions at 1.5 eV (upper panel) and at 2.5 eV (lower panel). The open circles are the experiments from reference [8].

earlier measurements of the group at Sophia University [8] (open circles) and the more recent data from the Australian group [1] (open triangles). The upper panel shows little change in the DCS with respect to the behaviour of Figure 4: near the resonant energy the experiments (which stop at 135°) indicate a rather flat dependence on the angle and possibly a forward peak limited to below 20°. The calculations also suggest a rather 'flat' distribution in the intermediate angular region but, since can go below 20° and beyond 135°, indicate there a marked increase of intensity in both the forward and backward angular ranges, as it should be expected for a trapped electron in a resonant situation where 'orbiting' is very likely to occur before break-up of the complex. As one goes above the resonance, however, (see lower panel of Fig. 5) the backward scattering markedly decreases while the forward scattering, dipole-controlled behaviour is returning to be important in the angular distributions: the calculations indeed follow very closely experiments at this low-energy away from resonance. The data in Figure 5 show an interesting 'dip' in the experimental cross-sections which is well reproduced by the calculations. To further analyse this point we show in Figure 6 the behaviour of the DCS at 3.5 and 4.0 eV. The experiments show even more markedly the drop in cross-section sizes as the angle approaches 20°, and our calculations also seem to follow rather realistically such interesting feature.

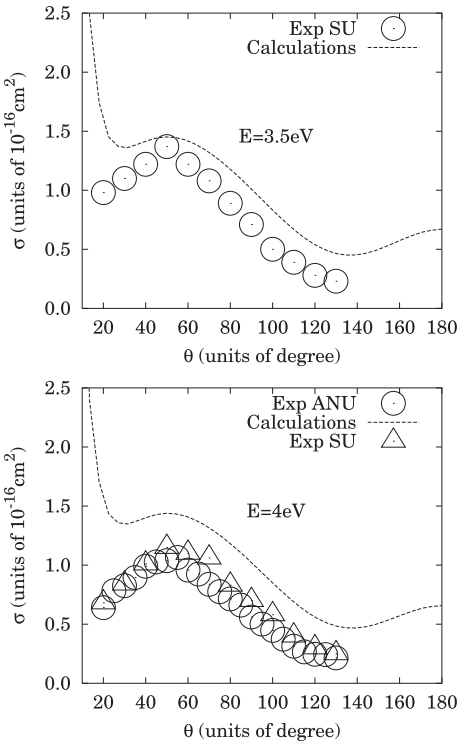

Fig. 6. Computed and measured angular distributions at 3.5 eV (upper panel) and at 4.0 eV (lower panel). The experiments are from reference [8].

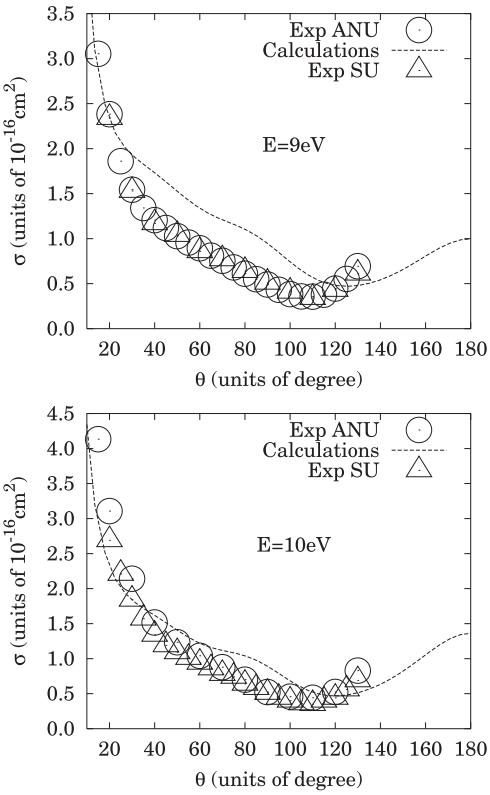

Fig. 7. Computed and measured electron scattered angular distributions at 9.0 eV (upper panel) and at 10.0 eV (lower panel). The experiments are from reference [8] (open triangles).

3.2 DCSs at higher collision energies

In order to contrast the scattered electron angular behaviour at energies away from the π^* shape resonance with those which exist around that resonance, we report in Figures 6 to 9 the DCS measured and computed over a very broad range of energies beyond the 2 eV value.

The data at 9.0 and 10.0 eV of Figure 7 exhibit, as before, a marked forward scattering behaviour and a reduction of the backward scattering peak: both features are clearly present in the experimental data and are confirmed by our calculations for both angular regions.

As one moves to yet higher collision energies, as shown by Figure 8, one notices a clear reduction of the backward peak and the persistence of the forward peaking for all angular distributions: it is also reassuring to see that the present calculations are reproducing the experiments remarkably well over the whole angular range.

Our calculations at the highest collision energies for which we have found experimental data [1,8] are shown in the three panels of Figure 9, where once more the computed data follow the experimental data very closely and reproduce very well, in both size and shape, the measured DCS for e^-N_2O scattering.

It is well-known that, as the collision energy increases the overall scattering process becomes dominated by static and exchange interactions and less by polarisation forces. Thus, we see that our calculations, which use exact static+exchange potentials, become increasingly in better

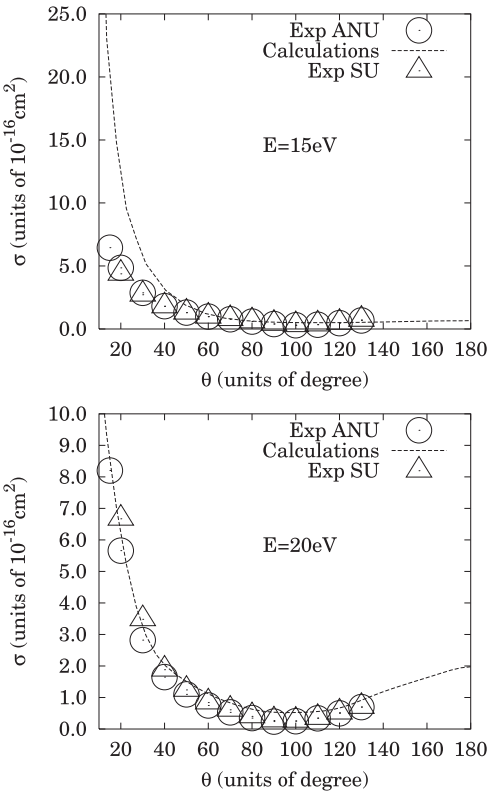

Fig. 8. Same as in Figure 7 but for two higher collision energies: at 15.0 eV (upper panel) and at 20.0 eV (lower panel).

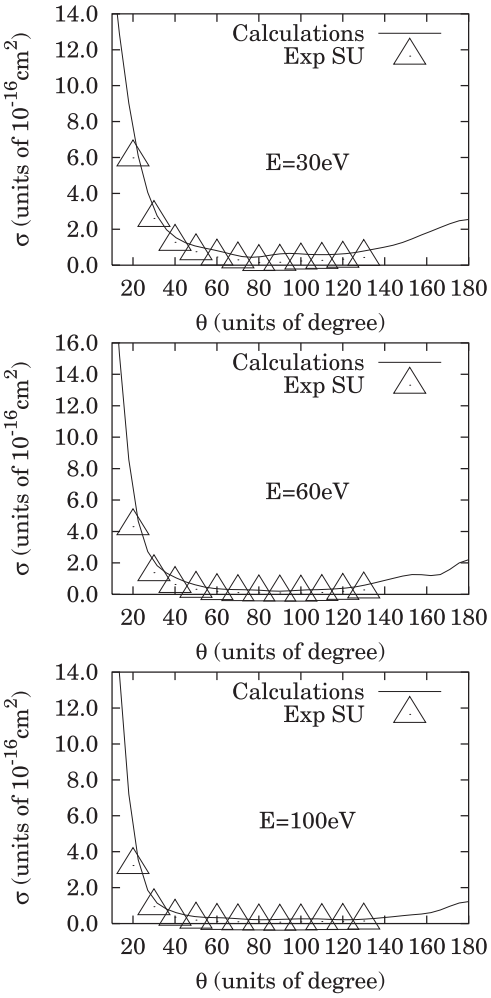

Fig. 9. Same as in Figure 7 but for different collision energies: 30.0 eV (upper panel); 60.0 eV (middle panel); 100.0 eV (lower panel).

agreement with the experiments as the collision energy goes up, as one sees in Figure 9.

4 Present conclusions

In this work we have analysed in detail the angular distributions recently measured for a gaseous polar molecule, the $N_2O(^1\Sigma)$, of interest in atmospheric chemistry and in the study of the chemistry of the ozone layer.

The objects of this study were several: we intended to test how well our treatment of the interaction forces could handle scattering from a polar molecule where the dipole scattering potential dominates the forward regions of the angular ranges. Our computed dipole is even larger than the experiments and therefore it poses even stronger numerical problems to forward scattering convergence, although does not affect the comparison with the available angles since they very seldom go to vanishing ϑ values at the energies available.

Further, we wanted to see if numerical convergence could be attained for a target molecule with a sizeable number of electrons as the present target, using an exact treatment of the static and exchange interactions. We have thus produced final cross-sections which were converged within 1% of their values. Finally, we wanted to test the reliability of our model description of correlation-polarization contributions by using it to analyse both the resonance region at low energies and the scattered electron angular distributions from 1.5 eV up to 100 eV. All these objects have been attained in the sense that our present results show that the chosen SECP interaction describes very adequately all scattering attributes for the title molecule and allows us to successfully compare them with available experiments.

The financial support of the Italian Ministry for University and Research (MUIR) through the PRIN 2004 project and the FIRB 2002 project is gratefully acknowledged. We also thank the COST project EIPAM for supporting a visit of T.S. to the laboratory in Rome.

References

1. M. Kitajiama, Y. Sakamato, R.J. Gulley, M. Hoshino, J.C. Gibson, H. Tanaka, S.J. Buckmann, J. Phys. B **33**, 1687 (2000)
2. C. Winstead, V. McKoy, Phys. Rev. A **57**, 3589 (1998)
3. B.K. Sarpal, K. Pfingst, B.M. Nestmann, S.D. Peyerimhoff, J. Phys. B **29**, 857 (1996)
4. L.A. Morgan, C.J. Gillan, J. Tennyson, X. Chen, J. Phys. B **30**, 4087 (1997)
5. C. Szmytowski, K. Maciag, G. Karwasz, D. Filipovic, J. Phys. B **22**, 525 (1989)
6. A. Zecca, I. Lazzizzera, M. Krauss, C.E. Kuyatt, J. Chem. Phys. **61**, 4560 (1974)
7. A. Zecca, I. Lazzizzera, M. Krauss, C.E. Kuyatt, Phys. Rev. A **25**, 129 (1993)
8. M. Kitajiama, Y. Sakamato, S. Watanabe, S. Suzuki, T. Ishikawa, T. Tanaka, M. Kimura, Chem. Phys. Lett. **309**, 414 (1999)
9. Cz. Szmytkowski, G. Karwasz, K. Maciag, Chem. Phys. Lett. **107**, 481 (1984)
10. Ch.K. Kwan, Y.-F. Hsieh, W.E. Kauppila, S.J. Smith, T.S. Stein, M.N. Uddin, Phys. Rev. Lett. **279**, 2083
11. F.A. Gianturco, T. Stoecklin, J. Phys. B **27**, 5903 (1994)
12. A. Jain, D.W. Norcross, Phys. Rev. A **32**, 1341 (1985)
13. E.g. see: J.S. Bell, E.J. Squires, Phys. Rev. Lett. **3**, 205 (1977)
14. T.H. Dunning Jr, P.J. Hay, *Modern Theoretical Chemistry*, edited by H.F. Schaefer III (Plenum Publ. Co., New York, 1976), Vol. 3
15. T.M. Rescigno, A.E. Orel, Phys. Rev. A **24**, 1267 (1981)
16. T.M. Rescigno, A.E. Orel, Phys. Rev. A **25**, 2402 (1982)
17. R. Launier, T.K. Bose, Can. J. Phys. **59**, 639 (1981)
18. F.J. Lovas, J. Phys. Chem. Ref. Data **7**, 1628 (1978)
19. N.T. Padial, D.W. Norcross, Phys. Rev. A **29**, 1590 (1984)
20. E.g. see: Y. Itikawa, Theor. Chem. Acc. **105**, 123 (2000)